inorganics

MDPI

Article

Direct Synthesis of $LiAlH_4$ from Ti-Doped Active LiAl Alloy

Yan Chu [1,†], Shiwei Fang [1,†], Yingjue Chen [1], Xiaoqi Zhang [1], Jie Zheng [1], Zhenglong Li [1], Wubin Du [1], Wengang Cui [1], Jian Miao [1], Yaxiong Yang [1,*], Yongfeng Liu [2], Mingxia Gao [2] and Hongge Pan [1,2,*]

[1] Institute of Science and Technology for New Energy, Xi'an Technological University, Xi'an 710021, China; cy15771817067@163.com (Y.C.); fangshiwei@st.xatu.edu.cn (S.F.); 19197164082@163.com (Y.C.); 16635432190@163.com (X.Z.); 18870337197@163.com (J.Z.); lizhenglong@xatu.edu.cn (Z.L.); msedwb@zju.edu.cn (W.D.); cuiwengang@xatu.edu.cn (W.C.); miaojian@xatu.edu.cn (J.M.)

[2] State Key Laboratory of Silicon Materials and School of Materials Science and Engineering, Zhejiang University, Hangzhou 310027, China; mselyf@zju.edu.cn (Y.L.); gaomx@zju.edu.cn (M.G.)

* Correspondence: yangyaxiong@xatu.edu.cn (Y.Y.); honggepan@zju.edu.cn or hgpan@zju.edu.cn (H.P.)

† These authors contribute equally to this work.

Abstract: $LiAlH_4$, characterized by high hydrogen capacity and metastable properties, is regarded as a promising hydrogen source under mild conditions. However, its reversible regeneration from dehydrogenated production is hindered thermodynamically and kinetically. Herein, we demonstrate an active Li–Al–Ti nanocrystalline alloy prepared by melt spinning and cryomilling to enable directly synthesizing nano-$LiAlH_4$. Due to the non-equilibrium preparation methods, the grain/particle size of the alloy was reduced, stress defects were introduced, and the dispersion of the Ti catalyst was promoted. The refined Li–Al–Ti nanocrystalline alloy with abundant defects and uniform catalytic sites demonstrated a high reactivity of the particle surface, thereby enhancing hydrogen absorption and desorption kinetics. Nano-$LiAlH_4$ was directly obtained by ball milling a 5% Ti containing Li–Al–Ti nanocrystalline alloy with a grain size of 17.4 nm and Al_3Ti catalytic phase distributed under 20 bar hydrogen pressure for 16 h. The obtained $LiAlH_4$ exhibited room temperature dehydrogenation performance and good reversibility. This finding provides a potential strategy for the non-solvent synthesis and direct hydrogenation of metastable $LiAlH_4$ hydrogen storage materials.

Keywords: hydrogen storage material; $LiAlH_4$; LiAl alloy; hydrogenation; kinetics; reversibility

check for updates

Academic Editors: Chao-Ming Huang and Guan-Ting Pan

Received: 19 January 2025
Revised: 20 February 2025
Accepted: 24 February 2025
Published: 1 March 2025

Citation: Chu, Y.; Fang, S.; Chen, Y.; Zhang, X.; Zheng, J.; Li, Z.; Du, W.; Cui, W.; Miao, J.; Yang, Y.; et al. Direct Synthesis of $LiAlH_4$ from Ti-Doped Active LiAl Alloy. *Inorganics* **2025**, *13*, 74. https://doi.org/10.3390/inorganics13030074

Copyright: © 2025 by the authors. Licensee MDPI, Basel, Switzerland. This article is an open access article distributed under the terms and conditions of the Creative Commons Attribution (CC BY) license (https://creativecommons.org/licenses/by/4.0/).

1. Introduction

Hydrogen is regarded as a critical carrier for achieving low-carbon energy transition due to its zero-carbon emission properties. However, because of hydrogen's ultra-low density and high diffusivity, the development of safe and efficient hydrogen storage technologies remains a major bottleneck for its large-scale application [1–4]. Solid-state hydrogen storage materials with high safety, high hydrogen storage density, and convenient transportability have emerged as a highly promising solution [5,6]. Among these materials, $LiAlH_4$ with a high hydrogen capacity (gravimetric: 10.5 wt%, volumetric: 96.6 $g{\cdot}L^{-1}$) and relatively moderate dehydrogenation temperature (~180 °C) has been extensively studied [7–14]. Nevertheless, the dehydrogenation process is accompanied by poor reversibility, severely limiting the potential of $LiAlH_4$ for cyclic applications and direct synthesis [15].

The decomposition of $LiAlH_4$ is generally accepted to proceed through three distinct steps ($LiAlH_4 \rightarrow Li_3AlH_6 \rightarrow LiH/Al \rightarrow LiAl$), with the initial step being an exothermic reaction (-10 $kJ{\cdot}mol^{-1}{\cdot}H_2$), rendering the regeneration of $LiAlH_4$ thermodynamically

unfavorable [16,17]. At ambient temperature, the direct hydrogenation of Li_3AlH_6 to $LiAlH_4$ requires hydrogen pressures exceeding 10^3 bar [18,19]. Only part of Li_3AlH_6 can be reversibly formed without $LiAlH_4$ when LiH/Al hydrogenation is performed with a titanium-based catalyst [20–23]. Furthermore, sluggish hydrogenation kinetics impose stringent synthesis conditions [20–23]. One strategy for regulating reaction thermodynamics is stabilizing $LiAlH_4$ by forming a complex with the ether (THF, Et_2O, Me_2O) [24–27]. In 1947, $LiAlH_4$ was first successfully achieved via the reaction of LiH with $AlCl_3$ in an ether solution [28]. This kind of liquid-phase synthesis method to stabilize $LiAlH_4$ by forming complexes with ethers is a feasible synthesis strategy. In addition, additional active sites, heterogeneous interfacial reactions, and $[AlH_4]^-$ nucleation can be promoted by the introduction of a catalyst, thereby improving the hydrogen absorption and desorption kinetics of metal hydrides [29–36]. Nevertheless, liquid-phase synthesis suffers complicated subsequent purification because of extensive organic solvent use. Therefore, a possible greener solid-phase synthesis method should urgently be explored and developed.

LiAl alloy, the fully dehydrogenated phase of $LiAlH_4$, crystallizes in a NaTl-type structure (B32), where Li and Al are mixed at the atomic level in a 1:1 ratio, which shows theoretical advantages in hydrogenation to form $LiAlH_4$. Moreover, metallic Ti, as an effective metal catalyst for aluminum hydride, can be flexibly introduced into the alloy preparation. However, given the low solubility of Ti in Al (only 0.2 at%) and its immiscibility with Li [37], ensuring the uniform dispersion of Ti within the LiAl alloy matrix presents a critical technical challenge [37,38]. Herein, two non-equilibrium preparation methods, melt spinning and cryomilling, were combined to effectively reduce the alloy grain/particle size and promote the uniform dispersion of the Ti catalyst. A Li–Al–Ti nanocrystalline alloy with a grain size of 17.4 nm and Al_3Ti catalytic phase dispersive distribution was successfully prepared. Nano-$LiAlH_4$ could be directly synthesized by the Li–Al–Ti alloy with the addition of 5% Ti through ball milling for 16 h under a hydrogen pressure of 20 bar. The obtained $LiAlH_4$ exhibited room temperature dehydrogenation performance and good reversibility.

2. Results and Discussion

The lithium–aluminum–titanium (denoted as LAT) alloys were prepared by suspension smelting, melt spinning, and cryomilling techniques, as schematically illustrated in Figure 1a. Firstly, lithium foils, aluminum granules, and titanium granules were induced to melt into an alloy (Figure 1b) with an atomic ratio of 1:1:0.037 (the mass ratio of titanium in the alloy was 5 wt%). The alloy flakes (Figure 1c) with different cooling rates were obtained by controlling the rotation speed of the copper roller in a vacuum chamber. In this experiment, the copper roller speed varied between 0, 2000, and 4000 rpm, and the samples obtained were denoted as LAT–b (the as–cast alloy), LAT–2000, and LAT–4000. Then, the obtained alloy flakes were cryomilled at liquid nitrogen temperature to obtain alloy powder (Figure 1d) as active LAT alloys, which were denoted as LAT–b–CM, LAT–2000–CM, and LAT–4000–CM, respectively.

The X-ray diffraction (XRD) patterns of LAT alloys prepared with different cooling rates are displayed in Figure 2. It was found that after adding 5 wt% of metallic Ti to the LiAl alloy, the ternary alloy contains two phases, the characteristic reflections of LiAl dominate the XRD profile, along with a small number of diffraction peaks of Al_3Ti. It is worth noting that the intensities of the LiAl alloy diffraction peaks decreased while the diffraction peaks of the Al_3Ti phases became stronger as the rotational speed of the copper roll increased. Only the (103) crystal plane diffraction peak of the Al_3Ti phase was observed in the LAT–b sample. With the increase in cooling rate, other diffraction peaks of the Al_3Ti phase could be further detected in the XRD spectra of the LAT–2000 and LAT–4000 samples.

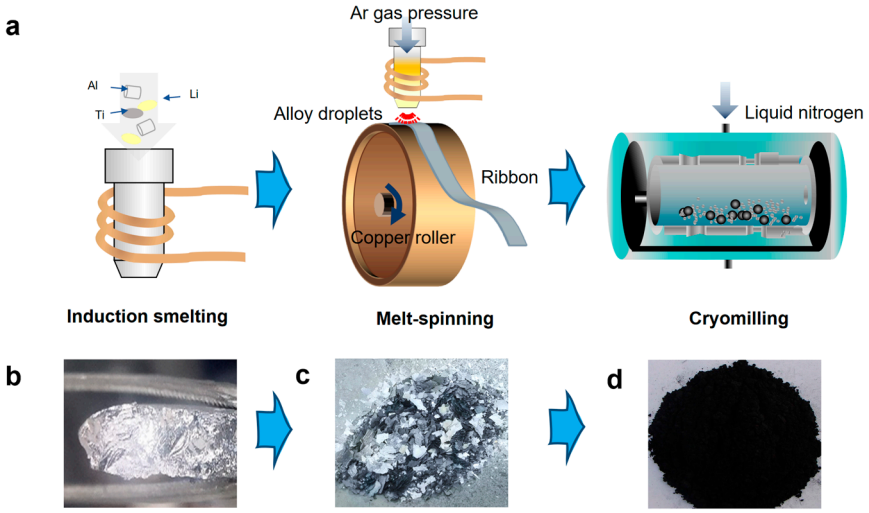

Figure 1. (**a**) Schematic diagram of the preparation process of active LAT alloys; optical photographs of (**b**) as-cast alloy by induction smelting, (**c**) alloy flakes by melt spinning, and (**d**) alloy powder after cryomilling.

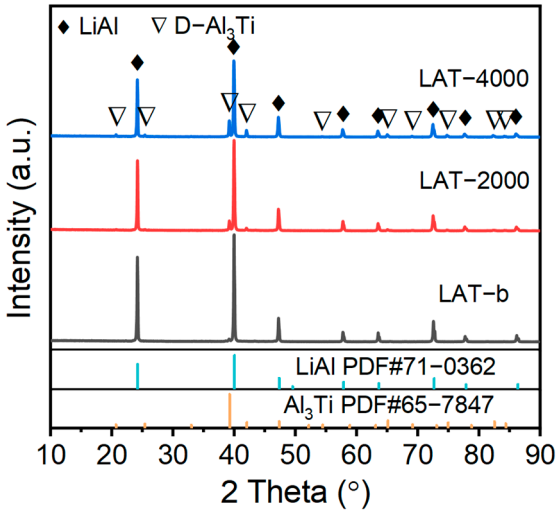

Figure 2. XRD patterns of LAT–b, LAT–2000, and LAT–4000 alloy flakes.

The morphology of the LAT alloy prepared at different rotational speeds is demonstrated as shown in Figure 3a–c. A relatively smooth and homogeneous surface morphology was observed in the as-cast alloy LAT–b. For the LAT–2000 alloy flakes, two phases with different contrasts were observed: the substrate was 1–3 μm dark contrast spherical particles with some ~10 μm bright contrast rectangular lamellas embedded (Figure 3b). When the rotational speed of the copper roller was increased to 4000 rpm, the high contrast phases in the obtained LAT–4000 sample were transformed into particles with a size of 5~8 μm (Figure 3a). The elemental distribution of Ti in the three alloys under different cooling rates was further characterized through energy-dispersive X-ray spectroscopy (EDX) mapping analysis (Figure 3d–f) and backscattering electron (BSE) imaging (Figure 3g–i). According to the EDX spectra, the alloy was mainly composed of Al and Ti. Owing to the limited solubility of Ti in Al alloys (0.2 at.%), the as-cast LAT-b alloy exhibited significant Ti segregation, with distinct Ti-depleted and Ti-enriched regions (Figure 3d,g). In Ti-depleted regions, finer Al_3Ti grains were observed (Figure 3d), whereas Ti-rich regions contained coarser particles (Figure 3g, displaying brighter contrast due to the higher atomic number of Ti). In the melt-spun LAT–2000 alloy flake, the distribution of Ti elements coincided with the rectangular lamellae structure with high contrast (Figure 3e,h). Similarly, in the

LAT–4000 alloy, Ti was predominantly concentrated in high-contrast particulate regions (Figure 3f,i). Combined with XRD analysis, the bright rectangular lamellae in LAT–2000 and the bright particles in LAT–4000 were identified as the Al_3Ti phase, while the dark, fine-grained matrix corresponded to the LiAl alloy phase. Notably, as the cooling rate increased, the Al_3Ti phase distribution became more homogeneous, accompanied by a reduction in grain size.

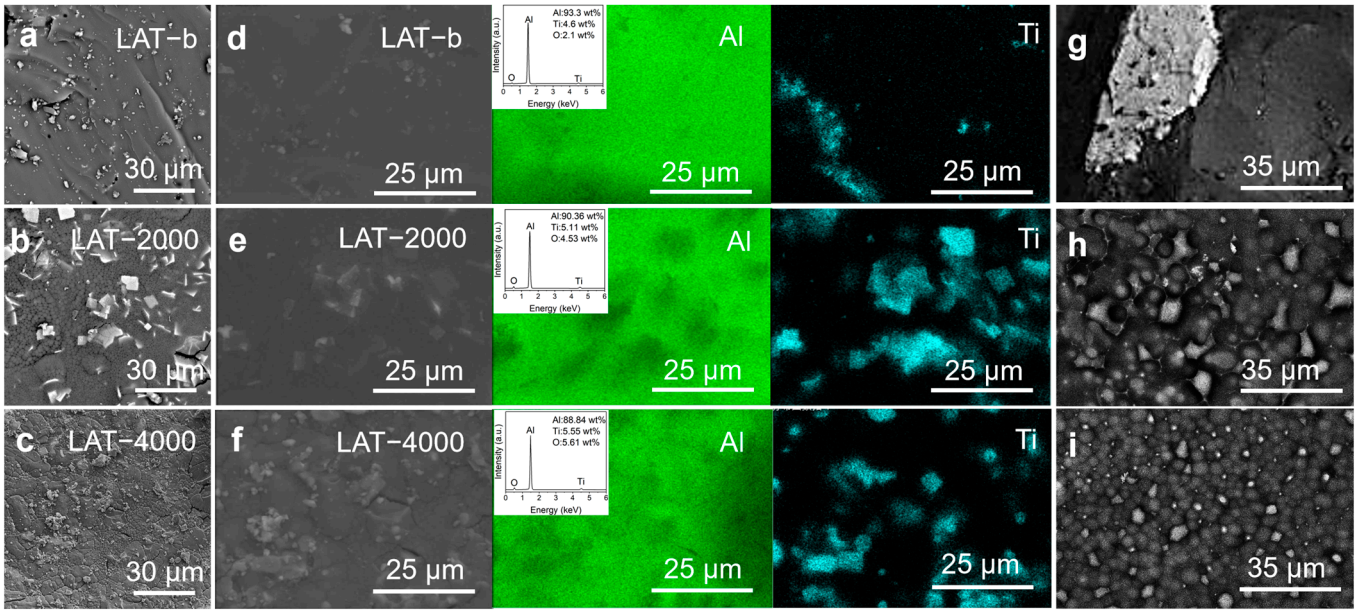

Figure 3. SEM of (**a**) LAT-b, (**b**) LAT-2000, and (**c**) LAT-4000; corresponding (**d**–**f**) EDX mapping (**g**–**i**) corresponding BSE images.

In the as-cast alloy, large metal grains and inhomogeneous phase distribution existed due to the slow cooling of the high-temperature metal liquid in the crucible. During the melt spinning process, the cooling rate increased as the copper roll speed increased to 2000 rpm. The Al_3Ti with a higher melting point (1200 °C) [39] in LAT–2000 nucleated preferentially, which provided the nucleation site for the grain refinement of the LiAl alloy. At this time, Al_3Ti phases presented rectangular lamellar structure due to a moderate cooling rate [40] and were embedded in the LiAl alloy matrix. When the copper roller speed increased to 4000 rpm, the nucleation rate of Al_3Ti in the LAT–4000 sample was further accelerated due to the higher cooling rate, and the grain refinement of the LiAl alloy was also promoted. The LAT–4000 alloy with irregular Al_3Ti particles embedded in a small-particle LiAl alloy matrix was obtained. By the non-equilibrium preparation method, the grain size of the LiAl alloy was refined and the catalyst phase Al_3Ti was evenly distributed in the alloy phase [41], which is of critical importance for improving the hydrogen storage kinetics of Ti-doped LiAl alloy.

In order to further refine the alloy particle and grain size, the LAT–b, LAT–2000, and LAT–4000 samples were cryomilled for 1 h, and the as prepared samples were noted as LAT–b–CM, LAT–2000–CM, and LAT–4000–CM, respectively. XRD profiles of the LAT alloys after cryomilling show the obvious broadening of the diffraction peak and decreasing of the diffraction intensity (Figure 4a), implying that the grains of the alloy were obviously refined after freezing ball milling, and a large number of stress–strain and other defects were introduced [42,43]. The grain size and strain of the alloy were calculated via the Williamson–Hall method [44]. As shown in Figure 4b, the grain sizes of LAT–b–CM, LAT–2000–CM, and LAT–4000–CM are 34.4, 20.5, and 17.4 nm, respectively. In addition, the microstrain of all samples reached ~0.4% owing to the severe plastic deformation induced by cryomilling.

It is worth pointing out that the Al_3Ti phase in the alloys changed from the tetragonal structure (PDF#65–7847) to the metastable simple cubic structure (PDF#49–1446) after cryomilling [45]. Further scanning electron microscope (SEM) observations revealed that after 1 h of cryomilling, the alloy flakes were transformed into small near-spherical alloy particles, and the particle size of the alloys was reduced to less than 5 μm (Figure 4c–e). Moreover, the particle size distribution of LAT–4000–CM is more uniform (Figure 4e). The transmission electron microscope (TEM) results further confirm that the element Ti is uniformly dispersed in the alloy particles of the LAT–4000–CM sample after the cryomilling (Figure 4f). These results demonstrate the significant grain/particle refinement, Al_3Ti phase transformation, and Ti element uniform distribution in the alloy particles after cryomilling treatment, leading to the formation of highly active Li–Al–Ti alloy powder.

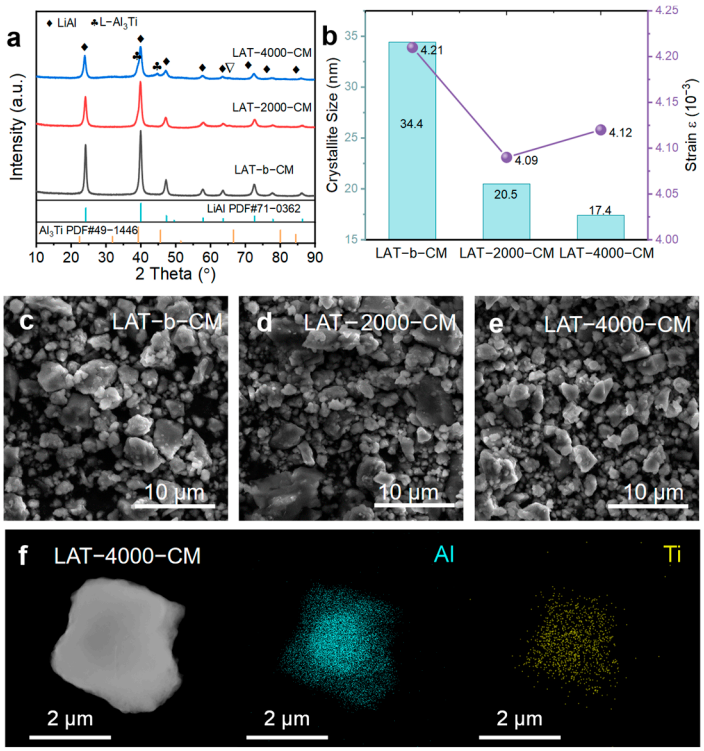

Figure 4. (**a**) XRD patterns and (**b**) corresponding crystallite size and strain of LAT–b–CM, LAT–2000–CM, and LAT–4000–CM; SEM images of (**c**) LAT–b–CM, (**d**) LAT–2000–CM, and (**e**) LAT–4000–CM, respectively; (**f**) TEM and corresponding EDX mapping of LAT–4000–CM.

The active alloy powders, after being cryomilled, were hydrogenated via ball milling for 16 h under 20 bar hydrogen pressure. The hydrogenated samples were labeled as LAT–b–CM–H, LAT–2000–CM–H, and LAT–4000–CM–H. The XRD patterns (Figure 5a) show that crystalline phases of LiH and Al appeared in all hydrogenated samples, indicating that the same reaction, $2LiAl + H_2 \rightarrow 2LiH + 2Al$, occurred during ball milling due to the favorable hydrogen affinity of Li [46]. The non-isothermal hydrogen desorption results are shown in Figure 5b, LAT–4000–CM–H began to desorb at room temperature ~25 °C, while LAT–b–CM–H and LAT–2000–CM–H started at approximately 40 °C. Upon heating to 180 °C, about 0.25, 0.44, and 0.58 wt% H_2 were desorbed by LAT–b–CM–H, LAT–2000–CM–H, and LAT–4000–CM–H, respectively, and after being further heated to 300 °C, 0.32, 0.60, and 0.79 wt% dehydrogenation capacities were obtained. The LAT–4000–CM–H sample exhibited a low initial desorption temperature and better hydrogen storage capability within 300 °C. The mass spectrum of LAT–4000–CM–H (Figure 5c) showed three desorption peaks at 124, 404, and about 500 °C, respectively, which further confirmed that the gas released in the low

temperature (<180 °C) was hydrogen. Combined with the XRD results, the produced LiH with high thermal stability is responsible for the dehydrogenation behavior above 380 °C (Figure 5a,b). X-ray photoelectron spectroscopy (XPS) characterization was further used to analyze the possible hydrogenation products of the alloy powder after hydrogenation. As shown in Figure 5d, the survey spectra of LAT–4000–CM–H indicated the presence of Li, Al, and oxide species. Although the vacuum level was strictly controlled throughout the experiment, and all samples were stored and transferred without exposure to water or oxygen, substantial amounts of lithium oxides and aluminum oxides were inevitably generated on the surfaces of the hydrogenated products due to the high chemical activity of the Li–Al–Ti alloy powders [47–50]. The presence of characteristic diffraction peaks for oxidizing species of aluminum and lithium (primarily composed of Al_2O_3 and Li_2O) between 30 and 35 degrees in the XRD pattern provides additional evidence to support this observation (Figure 5a). In the Al 2p spectra of the LAT–4000–CM–H sample (Figure 5e), four distinct peaks were observed at 74.9 eV, 74.1 eV, 72.7 eV, and 72.4 eV, corresponding to the binding energies of Al_2O_3, $LiAlH_4$ [8], Al, and Al_3Ti [51], respectively. It indicates that $LiAlH_4$ formed on the particle surface under mechanical chemical forces with Al_3Ti being catalytic, which contributes to the unique low-temperature hydrogen desorption behavior beginning at room temperature (Figure 5b).

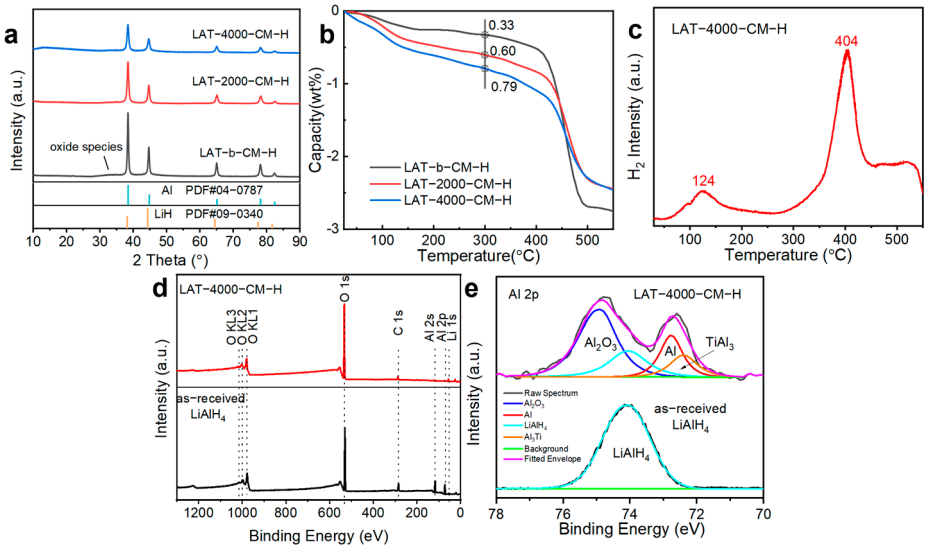

Figure 5. (**a**) XRD patterns and (**b**) Non-isothermal dehydrogen curves of LAT–b–CM–H, LAT–2000–CM–H, LAT–4000–CM–H samples; (**c**) hydrogen mass spectrum of LAT–4000–CM–H sample; (**d**) survey XPS spectra, and (**e**) Al 2p XPS spectra of LAT–4000–CM–H and as-received $LiAlH_4$.

According to the above hydrogenation properties of LAT alloys with different cooling rates, it can be seen that the LAT–4000–CM samples with small grain/particle sizes and uniform distribution of the Ti catalyst demonstrated better hydrogenation reaction ability. To compare the key roles of cooling rate, Ti addition, and defect-rich metastable structure on the hydrogenation kinetics of LiAl alloy, the as-cast LiAl alloy (LA–b) without a catalyst was prepared by direct melting. The structure and hydrogen ab/desorption properties of LA–b and LAT–4000–CM samples were compared. The XRD pattern confirmed that LA–b had a pure NaTl–type crystal structure (PDF#71–0362) and a sharp diffraction peak (Figure 6a). The calculated grain size of LA–b was about 139.3 nm, which is 10 times that of the Ti-doped LAT–4000–CM treated by melt spinning and cryomilling (Figure 4b, 17.4 nm).

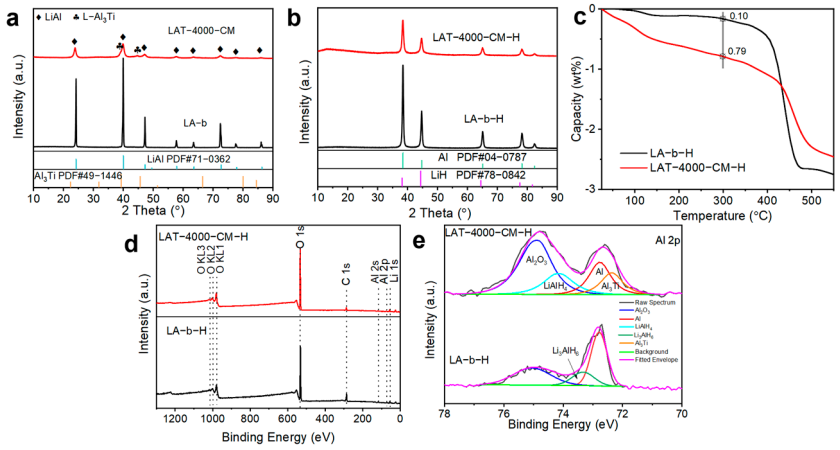

Figure 6. (**a**) XRD patterns of LAT–4000–CM and LA–b alloy, (**b**) XRD patterns, (**c**) non-isothermal dehydrogen curves, (**d**) survey XPS spectra, and (**e**) Al 2p XPS spectra of LAT–4000–CM–H and LA–b–H samples.

After the hydrogenation reaction ball milling at 20 bar hydrogen pressure for 16 h, only diffraction peaks of LiH and Al were observed in both obtained products LA–b–H and LAT–4000–CM–H (Figure 6b). However, as shown in the non-isothermal hydrogen desorption results in Figure 6c, there were significant differences in their hydrogen dehydrogenation behaviors. LA–b–H began hydrogen desorption at 98 °C, and only ~0.10 wt% was released when heating up to 300 °C, while LAT–4000–CM–H released hydrogen at room temperature (25 °C) and the dehydrogenation capacity at 300 °C was determined to be 0.79 wt%, nearly 8 times that of LA–b–H. These results suggested that more aluminum hydrides were generated during the hydrogenation of LAT–4000–CM. The XPS survey spectra (Figure 6d) confirmed the presence of Li, Al, and oxide species in both the LA–b–H and LAT–4000–CM–H samples. Owing to the large grain/particle size, limited specific surface area, and relatively low chemical activity of the as-cast LA–b alloy, the extent of surface oxidation of Al in the samples (Figure 6e) was comparatively mild. Al 2p spectra of LAT–4000–CM–H and LA–b–H samples revealed that the surface of LA–b–H was mainly dominated by Al, and only trace amounts of thermodynamically stable Li_3AlH_6 were found, which is due to the poor interfacial reaction kinetics of as-cast LiAl alloy. However, for the LAT–4000–CM sample, which consists of Ti-doped LiAl nanocrystalline alloys, the hydrogenation reaction tends to directly produce nano-$LiAlH_4$. In this nanocrystalline alloy, Al_3Ti nanocatalysts are uniformly dispersed within the LiAl alloy matrix. These Al_3Ti particles serve as catalysts for hydrogen dissociation and recombination [39], while simultaneously generating numerous heterogeneous nucleation sites. During hydrogenation, hydrogen molecules dissociate into individual H atoms on the surface of the Al_3Ti nanocatalysts and initially gather around the heterogeneous nucleation sites formed by the Al_3Ti distribution [52–54]. The H atoms then diffuse and dissolve into the surrounding high-defect-state LiAl alloy nanocrystalline, leading to the formation of nano-$LiAlH_4$. The synergistic effects of the enhanced kinetics driven by these catalysts and heterogeneous nucleation sites, combined with the modulation of hydrogenation thermodynamics by the nanocrystalline and metastable defect-rich structures, collectively enable the direct hydrogenation formation of nano-$LiAlH_4$ from the Li–Al–Ti nanocrystalline alloy and its room-temperature hydrogen desorption behavior [6,55,56].

The reversibility of the aluminum hydride obtained from the hydrogenation of Ti-doped LiAl nanocrystalline alloys was further studied. The product of LAT–4000–CM–H dehydrogenated at 300 °C was subjected to 100 bar hydrogen pressure and held at 100 °C for 24 h. The non-isothermal hydrogen desorption results of the rehydrogenated product

are shown in Figure 7a, the sample still began hydrogen desorption at room temperature with 0.49 wt% hydrogen released when heated to 300 °C, maintaining 62% of the initial dehydrogenation capacity. We observed that oxides remain present both before and after hydrogen release (Figure 7b–d). In contrast to the dense Al_2O_3 layer in pure Al, which completely blocks hydrogen diffusion [57], the surface oxide layer of the Li–Al–Ti alloy consists of a mixture of lithium and aluminum oxides (Figure 7c,d). The multicomponent oxide layer, primarily composed of Al_2O_3 and Li_2O grains, serves a dual purpose: it protects the alloy and hydride from further oxidation, while its non-dense structure, combined with the presence of numerous oxide grain boundaries, facilitates potential pathways for hydrogen adsorption and diffusion during the processes of hydrogen absorption and desorption [58]. The high-resolution Al 2p XPS spectrum also confirmed that the surface of the product was rehydrogenated back to $LiAlH_4$ (Figure 7c), implying that the locally generated nano-$LiAlH_4$ on the alloy particle surface showed certain reversibility. The reported catalysts, including TiC [59], ZrC [59], TiN [59], $MnFe_2O_4$ [60], and K_2NiF_6 [61], doped with $LiAlH_4$ dehydrogenation products, had shown no reversibility for hydrogenation. The after-dehydrogenation absorption capacities of $LiAlH_4$ doped with 5 wt% nano Fe [62] and 7 wt% $NiTiO_3$@h-BN [23] were 0.5 wt% and 1 wt%, respectively, with only Li_3AlH_6 identified as the hydrogen absorption product. However, no reversible formation of $LiAlH_4$ was achieved. In contrast, nano-$LiAlH_4$ was directly obtained by ball milling a 5% Ti containing Li–Al–Ti nanocrystalline alloy under 20 bar hydrogen pressure for 16 h.

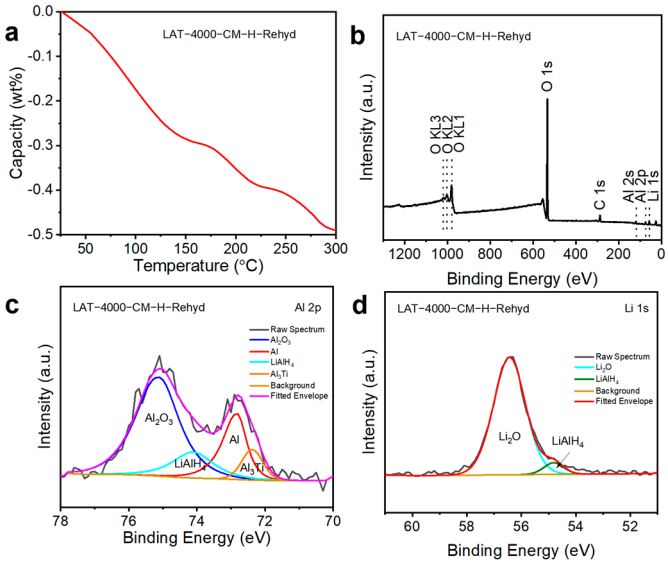

Figure 7. (**a**) Non-isothermal dehydrogen curves, (**b**) survey XPS spectra, (**c**) Al 2p XPS spectrum, and (**d**) Li 1s XPS spectrum of rehydrogenated LAT–4000–CM–H.

3. Materials and Methods

3.1. Preparation of the Li–Al–Ti Alloy

Lithium tablets (Φ13 mm, purity 99.99%, Xinjiang Nonferrous Metals Industry (Group) Co., Ltd. (Urumqi, China), aluminum granules (Φ6 × 3 mm, purity 99.999%, Zhongnuo Advanced Materials (Beijing) Technology Co., Ltd., Beijing, China), and titanium powder (Φ6 × 3 mm, purity 99.999%, Aladdin, Shanghai, China) were purchased and used as received without further purification. The titanium powder was pressed with a flake grinding tool and then put into a boron nitride crucible with lithium flakes and aluminum particles and transferred to a high-vacuum melting and quenching equipment. The chamber vacuum reached 10^{-3} bar, then the chamber was filled with argon gas to reach atmospheric pressure. The pressure of the injected molten cast was set to 2 bar, and the distance between

the copper rod and the crucible was adjusted to 1 mm. The rotational speeds of the copper rollers were adjusted to be 0, 2000, and 4000 rpm, and then the heating power was elevated until the granules in the crucible were in a molten state. Next, the cast melt was sprayed with argon to obtain Li–aluminum–titanium alloy flakes. A total of 1 g of the alloy flakes and 100 g of hardened steel balls was sealed in a 50 mL hardened steel vial; then, the vial was transferred to a Retsch CryoMill (Haan, Germany) and cryomilled at liquid nitrogen temperature (77 K) with 30 Hz impact frequency for 60 min. In a typical process, 20 min of pre-cooling was performed first to bring the temperature of the tank to the temperature of the liquid nitrogen, and then, ball milling was performed for 5 min to make the alloy with higher energy, with a break of 2 min to eliminate the heat generated in the process of the ball milling.

3.2. Synthesis of $LiAlH_4$ Through Hydrogen-Reactive Ball Milling

$LiAlH_4$ was prepared through hydrogen-reactive ball milling (HRBM) employing a planetary ball milling apparatus (QM–3SP4, Nanjing China). In an argon-atmosphere protected glove box, approximately 1 g of Li–Al–Ti flakes and 100 g of stainless-steel spherical grinding beads were filled into a custom-engineered milling vessel. Then, the jar underwent an evacuation process and was pressurized with hydrogen at 20 bar (purity 99.999%; Xi'an Tianhai Gas Co., Ltd., Xi'an, China). The ball milling speed was set to 400 rpm, the hydrogenated samples were obtained after 16 h of HRBM. For comparison, the as-cast LiAl alloy was hydrogenated by HRBM following an identical grinding process. All samples were handled within an argon-purged glove box (Lab2000, Etelux, Beijing, China, $H_2O < 0.1$ ppm; $O_2 < 0.1$ ppm).

3.3. Structure and Morphology Characterizations

X-ray diffraction, via a PANalytical X'Pert X-ray diffractometer sourced from the Netherlands and Cu Kα (λ = 0.15406 nm, 40 kV, 75 mA) radiation, was applied to characterize the crystal textures within a nitrogen-filled glove box (MBRAUN 200B, Bayern, Germany). Data acquisition was performed within a 2θ angular span ranging from 10° to 90°; a step interval of 0.02° was employed. A transmission electron microscope (TEM, Tecnai G2 F20, Waltham, MA, USA) and a scanning electron microscope (SEM, Hitachi SU–70, Ibaraki Prefecture, Japan) integrated with an energy-dispersive X-ray spectroscopy (EDX) and backscattered electron (BSE) system were employed to examine the microstructural features and elemental distributions of the samples. X-ray photoelectron spectroscopy (XPS, ThermoFisher ESCALAB Xi, Waltham, MA, USA) employing an Al Kα radiation source was utilized to characterize the elemental chemical states. The pass energy for the full spectra and Al–2p high–resolution spectra in the XPS measurements was set to 100 eV and 30 eV, respectively. The studied samples were subjected to XPS testing directly without any prior surface ion-etching.

3.4. Hydrogen Storage Property Measurements

The hydrogen desorption characteristics of the samples were evaluated with a meticulously calibrated Siever-type instrument. Experiments were conducted in a non-isothermal mode, wherein approximately 50–60 mg of the sample was loaded into a stainless-steel reactor and heated to a specified temperature at a rate of 2 °C/min under a vacuum of 10^{-2} Pa. The hydrogen absorption properties were measured isothermally. The dehydrogenated samples were heated to 100 °C under vacuum, and then 10 MPa H_2 was rapidly charged to start the hydrogenation. Hydrogen levels at the analyzer outlet were continuously monitored using a quadrupole mass spectrometer (Hiden HPR–20EGA, Cheshire, UK).

4. Conclusions

Through the high cooling rate of melting spinning, the grain size of 5% Ti containing Li–Al–Ti alloy was refined, and the LAT–4000 alloy flakes with a dispersed Al_3Ti catalyst phase were obtained. Further, by cryomilling for 1 h, the grain/particle size of LAT–4000–CM was reduced to ~17.4 nm/2.5 μm, ~0.4% microstrain was introduced, and the Ti element uniform distribution was further promoted. Owing to the enhancement of hydrogenation kinetics by the uniformly dispersed Al_3Ti catalyst phase and the regulation of hydrogenation reaction thermodynamics and kinetics by nanocrystalline and metastable defect-rich structure, $LiAlH_4$ could be directly formed by the high-activity LAT–4000–CM alloy powder via reactive milling under 20 bar hydrogen. The composite hydride containing nano-$LiAlH_4$ began hydrogen desorption at room temperature (25 °C) and the dehydrogenation capacity at 300 °C was determined to be 0.79 wt%. Furthermore, the locally generated nano-$LiAlH_4$ exhibited a certain reversibility due to the $LiAlH_4$ that was also obtained after rehydrogenation of the dehydrogenation product. Although the synthesized $LiAlH_4$ content was limited and the hydrogen storage capacity remained low, this finding provides a novel approach for the non-solvent synthesis of metastable $LiAlH_4$ at room temperature. Building on this, strategies such as multi-component alloying and interface modification could potentially further enhance the synthetic yield of $LiAlH_4$. Furthermore, by combining this method with liquid-phase synthesis assisted by organic solvents and replacing $LiH/AlCl_3$ with Li–Al–Ti alloy, the challenges associated with the removal of inert byproducts such as LiCl and NaCl might be mitigated, thereby optimizing the existing synthesis strategy for $LiAlH_4$.

Author Contributions: Conceptualization, Y.C. (Yan Chu) and Y.Y.; methodology, S.F.; validation, Y.C. (Yingjue Chen) and X.Z.; investigation, Y.C. (Yingjue Chen) and J.Z.; formal analysis, Z.L. and W.D.; writing—original draft preparation, Y.C. (Yan Chu) and S.F.; writing—review and editing, Y.Y., W.C., and Y.L.; visualization, W.D.; resources, J.M. and H.P.; supervision, M.G.; project administration, J.M.; funding acquisition, Y.Y., Z.L., and H.P. All authors have read and agreed to the published version of the manuscript.

Funding: This research was funded by the National Key Research and Development Program of China (2021YFB4000602), the National Natural Science Foundation of China (52271227, 52307250), the Natural Science Foundation of Zhejiang Province, PR China (LZ23E010002), the Two-chain integration key project of Shaanxi Province (2021LLRH-09), and the Key Research and Development Program of Shaanxi (S2024-YF-ZDXM-CY-0359, 2024GX-ZDCYL-04-06).

Data Availability Statement: The original contributions presented in this study are included in the article. Further inquiries can be directed to the corresponding authors.

Conflicts of Interest: The authors declare no conflicts of interest.

References

1. Zhao, P.C.; Deng, L.Q.; Sun, C.; Li, X.P.; Tian, X.Y.; Li, Z.; Sheng, W.C. New Insights into the Roles of Surface and Lattice Hydrogen in Electrocatalytic Hydrogen Oxidation. *ACS Catal.* **2025**, *15*, 1352–1362. [CrossRef]
2. Yang, Q.; Jia, X.; Qin, Z.; Ding, X.; Li, Y. Enhancements in Hydrogen Storage Properties of Magnesium Hydride Supported by Carbon Fiber: Effect of C–H Interactions. *Inorganics* **2024**, *12*, 273. [CrossRef]
3. Jensen, E.H.; Dornheim, M.; Sartori, S. Scaling up Metal Hydrides for Real-Scale Applications: Achievements, Challenges and Outlook. *Inorganics* **2021**, *9*, 37. [CrossRef]
4. Peru, F.; Payandeh, S.; Jensen, T.R.; Charalambopoulou, G.; Steriotis, T. Destabilization of the $LiBH_4$–$NaBH_4$ Eutectic Mixture through Pore Confinement for Hydrogen Storage. *Inorganics* **2023**, *11*, 128. [CrossRef]
5. Abdechafik, E.H.; Ousaleh, H.A.; Mehmood, S.; Baba, Y.F.; Bürger, I.; Linder, M.; Faik, A. An analytical review of recent advancements on solid-state hydrogen storage. *Int. J. Hydrogen Energy* **2024**, *52*, 1182–1193. [CrossRef]
6. Wang, L.; Aguey-Zinsou, K.F. Synthesis of $LiAlH_4$ Nanoparticles Leading to a Single Hydrogen Release Step upon Ti Coating. *Inorganics* **2017**, *5*, 38. [CrossRef]

7. Zhang, G.R.; Liu, J.X.; Wei, S.; Xu, F.; Sun, L.X.; Xia, Y.P.; Wang, H.H.; Wu, J.F.; Gao, Y.; Shao, Q.W.; et al. Thermally induced in situ fabrication of TiO_2/CN heterojunction dopant for enhancement of hydrogen storage properties of $LiAlH_4$. *J. Mater. Sci. Technol.* **2024**, *203*, 227–236. [CrossRef]
8. Pratthana, C.; Aguey-Zinsou, K.F. $LiAlH_4$ Nanoparticles Encapsulated within Metallic Titanium Shells for Enhanced Hydrogen Storage. *ACS Appl. Nano Mater.* **2022**, *5*, 16413–16422. [CrossRef]
9. Tena-García, J.R.; Osorio-Garcia, M.; Suárez-Alcántara, K. $LiBH_4$–VCl_3 and $LiAlH_4$–VCl_3 mixtures prepared in soft milling conditions for hydrogen release at low temperature. *Int. J. Hydrogen Energy* **2022**, *47*, 28046–28060. [CrossRef]
10. Bu, Y.T.; Sun, L.X.; Xu, F.; Luo, Y.M.; Zhang, C.C.; Wei, S.; Zhang, G.R.; Pan, H.G.; Zeng, J.L.; Cao, Z. Improved dehydrogenation of $LiAlH_4$ by Hollow 3D flower-like bimetallic composites M-NC@TiO_2 (M=Ni, Co, Fe, Cu). *Ceram. Int.* **2024**, *50*, 34251–34263. [CrossRef]
11. Bu, Y.T.; Sun, L.X.; Xu, F.; Wei, S.; Rosei, F.; Luo, Y.M.; Liu, Z.Y.; Liu, J.X.; Zhang, C.C.; Yao, Y. Highly active bimetallic MOF derivatives for improving the dehydrogenation performance of $LiAlH_4$. *J. Alloys Compd.* **2023**, *961*, 170897. [CrossRef]
12. Liu, Z.Y.; Liu, J.X.; Wei, S.; Xia, Y.P.; Cheng, R.G.; Sun, L.X.; Xu, F.; Huang, P.R.; Bu, Y.T.; Cheng, J.; et al. Improved Hydrogen Storage Properties and Mechanisms of $LiAlH_4$ Doped with Ni/C Nanoparticles Anchored on Large-Size $Ti_3C_2T_x$. *J. Alloys Compd.* **2023**, *931*, 167353. [CrossRef]
13. Ismail, M.; Ali, N.A.; Sazelee, N.A.; Suwarno, S.S. Catalytic effect of Al_2TiO_5 on the dehydrogenation properties of $LiAlH_4$. *Int. J. Hydrogen Energy* **2022**, *47*, 31903–31910. [CrossRef]
14. Pratthana, C.; Aguey-Zinsou, K.F. Surfactant Induced Synthesis of $LiAlH_4$ and $NaAlH_4$ Nanoparticles for Hydrogen Storage. *Appl. Sci.* **2022**, *12*, 4742. [CrossRef]
15. Leng, H.Y.; Xu, J.L.; Jiang, J.J.; Xiao, H.Y.; Li, Q.; Chou, K.-C. Improved dehydrogenation properties of $Mg(BH_4)_2{\cdot}2NH_3$ combined with $LiAlH_4$. *Int. J. Hydrogen Energy* **2015**, *40*, 8362–8367. [CrossRef]
16. Jain, I.P.; Jain, P.Y.; Jain, A. Novel hydrogen storage materials: A review of lightweight complex hydrides. *J. Alloys Compd.* **2010**, *503*, 303–339. [CrossRef]
17. Orimo, S.I.; Nakamori, Y.; Eliseo, J.R.; Züttel, A.; Jensen, C.M. Complex hydrides for hydrogen storage. *Chem. Rev.* **2007**, *107*, 4111–4132. [CrossRef]
18. Jang, J.W.; Shim, J.H.; Cho, Y.W.; Lee, B.J. Thermodynamic calculation of $LiH{\leftrightarrow}Li_3AlH_6{\leftrightarrow}LiAlH_4$ reactions. *J. Alloys Compd.* **2006**, *420*, 286–290. [CrossRef]
19. Ke, X.Z.; Chen, C.F. Thermodynamic functions and pressure-temperature phase diagram of lithium alanates by ab initio calculations. *Phys. Rev. B Condens. Matter Mater. Phys.* **2007**, *76*, 024112. [CrossRef]
20. Chen, J.; Kuriyama, N.; Xu, Q.; Takeshita, H.T.; Sakai, T. Reversible Hydrogen Storage via Titanium-Catalyzed $LiAlH_4$ and Li_3AlH_6. *J. Phys. Chem. B* **2001**, *105*, 11214–11220. [CrossRef]
21. Din, R.U.; Zhang, L.; Li, P.; Qu, X.H. Catalytic effects of nano-sized TiC additions on the hydrogen storage properties of $LiAlH_4$. *J. Alloys Compd.* **2010**, *508*, 119–128. [CrossRef]
22. Wei, S.; Liu, J.X.; Xia, Y.P.; Zhang, H.Z.; Cheng, R.G.; Sun, L.X.; Xu, F.; Huang, P.R.; Rosei, F.; Pimerzin, A.A.; et al. Remarkable catalysis of spinel ferrite XFe_2O_4 (X = Ni, Co, Mn, Cu, Zn) nanoparticles on the dehydrogenation properties of $LiAlH_4$: An experimental and theoretical study. *J. Mater. Sci. Technol.* **2022**, *111*, 189–203. [CrossRef]
23. Wei, S.; Liu, J.X.; Xia, Y.P.; Zhang, H.Z.; Cheng, R.G.; Sun, L.X.; Xu, F.; Bu, Y.T.; Liu, Z.Y.; Huang, P.R.; et al. Enhanced Hydrogen Storage Properties of $LiAlH_4$ by Excellent Catalytic Activity of $XTiO_3$@h-BN (X = Co, Ni). *Adv. Funct. Mater.* **2021**, *32*, 2110180. [CrossRef]
24. Graetz, J.; Wegrzyn, J.; Reilly, J.J. Regeneration of Lithium Aluminum Hydride. *J. Am. Chem. Soc.* **2008**, *130*, 17790–17794. [CrossRef] [PubMed]
25. Clasen, H. Alanat-Synthese aus den Elementen und ihre Bedeutung. *Angew. Chem.* **1961**, *73*, 322–331. [CrossRef]
26. Ashby, E.C.; Brendel, G.J.; Redman, H.E. Direct synthesis of complex metal hydrides. *Inorg. Chem.* **1963**, *2*, 499–504. [CrossRef]
27. Liu, X.; McGrady, G.S.; Langmi, H.W.; Jensen, C.M. Facile cycling of Ti-doped $LiAlH_4$ for high performance hydrogen storage. *J. Am. Chem. Soc.* **2009**, *131*, 5032–5033. [CrossRef]
28. Finholt, A.E.; Bond Jr, A.C.; Schlesinger, H.I. Lithium aluminum hydride, aluminum hydride and lithium gallium hydride, and some of their applications in organic and inorganic chemistry[1]. *J. Am. Chem. Soc.* **1947**, *69*, 1199–1203. [CrossRef]
29. Sazelee, N.A.; Ismail, M. Recent advances in catalyst-enhanced $LiAlH_4$ for solid-state hydrogen storage: A review. *Int. J. Hydrogen Energy* **2021**, *46*, 9123–9141. [CrossRef]
30. Zheng, X.P.; Li, P.; Qu, X.H. Engineering, Effect of additives on the reversibility of lithium alanate ($LiAlH_4$). *Rare Met. Mater. Eng.* **2009**, *38*, 766–769. [CrossRef]
31. Zheng, X.P.; Li, P.; Humail, I.S.; An, F.Q.; Wang, G.Q.; Qu, X.H. Effect of catalyst $LaCl_3$ on hydrogen storage properties of lithium alanate ($LiAlH_4$). *Int. J. Hydrogen Energy* **2007**, *32*, 4957–4960. [CrossRef]
32. Kojima, Y.; Kawai, Y.; Haga, T.; Matsumoto, M.; Koiwai, A. Direct formation of $LiAlH_4$ by a mechanochemical reaction. *J. Alloys Compd.* **2007**, *441*, 189–191. [CrossRef]

33. Zhang, C.M.; Wang, C.L.; Shi, Q.Y.; Wang, X.L.; Zhao, S.L.; Liang, L.; Wang, Q.S.; Wang, L.M.; Cheng, Y. Constructing Ni/CeO_2 synergistic catalysts into $LiAlH_4$ and AlH_3 composite for enhanced hydrogen released properties. *Appl. Catal. B Environ.* **2024**, *359*, 124521. [CrossRef]
34. Sazelee, N.A.; Ali, N.A.; Liu, H.; Ismail, M. Improving the desorption properties of $LiAlH_4$ by the addition of $Ni_{0.6}Zn_{0.4}O$. *Int. J. Hydrogen Energy* **2024**, *56*, 543–551. [CrossRef]
35. Ali, N.A.; Nasef, M.M.; Jalil, A.A.; Ismail, M. Zn_2TiO_4 synthesized via solid-state method and its effects on dehydrogenation properties of $LiAlH_4$. *Int. J. Hydrogen Energy* **2024**, *50*, 484–494. [CrossRef]
36. Zhang, C.M.; Liang, L.; Zhao, S.L.; Wu, Z.J.; Wang, S.H.; Yin, D.M.; Wang, Q.S.; Wang, L.M.; Wang, C.L.; Cheng, Y. Dehydrogenation behavior and mechanism of $LiAlH_4$ adding nano-CeO_2 with different morphologies. *Nano Res.* **2023**, *16*, 9426–9434. [CrossRef]
37. Gu, J.L.; Duan, F.H.; Liu, S.D.; Cha, W.H.; Lu, J. Phase Engineering of Nanostructural Metallic Materials: Classification, Structures, and Applications. *Chem. Rev.* **2024**, *124*, 1247–1287. [CrossRef]
38. Kotelnikova, A.; Zubar, T.; Vershinina, T.; Panasiuk, M.; Kanafyev, O.; Fedkin, V.; Kubasov, I.; Turutin, A.; Trukhanov, S.; Tishkevich, D.; et al. The Influence of Saccharin Adsorption on NiFe Alloy Film Frowth Mechanisms during Electrodeposition. *RSC Adv.* **2022**, *12*, 35722–35729. [CrossRef]
39. Hu, K.S.; Zou, C.M.; Wang, H.W.; Wei, Z.J. The role of in-situ Al_3Ti formed during solidification in improving the high-temperature properties of Al-Cu alloy. *Mater. Sci. Eng. A* **2024**, *902*, 146585. [CrossRef]
40. Watanabe, Y.; Mihara-Narita, M.; Sato, H. Grain Refinement of Cast Aluminum by Heterogeneous Nucleation Site Particles with High Lattice Matching. *Mater. Trans.* **2023**, *64*, 1083–1097. [CrossRef]
41. Ascencio de la Cruz, L.A.; Flores-Zúñiga, H.; Alvarado-Hernández, F.; Camarillo-Garcia, J.P. Microstructure and thermal characterization of $Ni_{50}Mn_{33}Cr_{10}In_7$ alloy in bulk and ribbons. *MRS Adv.* **2025**, 1–6. [CrossRef]
42. Klassen, T.; Oehring, M.; Bormann, R. The early stages of phase formation during mechanical alloying of Ti–Al. *J. Mater. Res.* **1994**, *9*, 47–52. [CrossRef]
43. Turchenko, V.A.; Trukhanov, S.V.; Kostishin, V.G.; Damay, F.; Porcher, F.; Klygach, D.S.; Vakhitov, M.G.; Matzui, L.Y.u.; Yakovenko, O.S.; Bozzo, B.; et al. Impact of In^{3+} Cations on Structure and Electromagnetic State of M-Type Hexaferrites. *J. Energy Chem.* **2022**, *69*, 667–676. [CrossRef]
44. Kalita, A.; Kalita, M.P.C. Nanostructures, Williamson-Hall analysis and optical properties of small sized ZnO nanocrystals. *Phys. E* **2017**, *92*, 36–40. [CrossRef]
45. Balema, V.P.; Wiench, J.W.; Dennis, K.W.; Pruski, M.; Pecharsky, V.K. Titanium catalyzed solid-state transformations in $LiAlH_4$ during high-energy ball-milling. *J. Alloys Compd.* **2001**, *329*, 108–114. [CrossRef]
46. Li, X.X.; Wang, J.S.; Miao, Y.S.; Li, Q.; Xue, C.P.; Yang, X.H. In-situ study on the effect of Li concentration on hydrogen microporosity evolution in Al-Li alloys by synchrotron X-ray radiography. *J. Alloys Compd.* **2024**, *1008*, 176810. [CrossRef]
47. Kim, S.H.; Hui, K.N.; Kim, Y.J.; Lim, T.S.; Yang, D.Y.; Kim, K.B.; Kim, Y.J.; Jang, G.J.; Yang, S.S. Fabrication of Pre-Alloyed Al-Li Powders with High Li Content via Thermal Dehydrogenation of LiH and Rapid Solidification Process. *Mater. Des.* **2016**, *94*, 159–165. [CrossRef]
48. Ares, J.R.; Aguey-Zinsou, K.F.; Porcu, M.; Sykes, J.M.; Dornheim, M.; Klassen, T.; Bormann, R. Thermal and Mechanically Activated Decomposition of $LiAlH_4$. *Mater. Res. Bull.* **2008**, *43*, 1263–1275. [CrossRef]
49. Andrei, C.M.; Walmsley, J.C.; Brinks, H.W.; Holmestad, R.; Blanchard, D.; Hauback, B.C.; Botton, G.A. Analytical Electron Microscopy Studies of Lithium Aluminum Hydrides with Ti- and V-Based Additives. *J. Phys. Chem. B* **2005**, *109*, 4350–4356. [CrossRef]
50. Trukhanov, S.V.; Trukhanov, A.V.; Vasiliev, A.N.; Balagurov, A.M.; Szymczak, H. Magnetic State of the Structural Separated Anion-Deficient $La_{0.70}Sr_{0.30}MnO_{2.85}$ Manganite. *J. Exp. Theor. Phys.* **2011**, *113*, 819–825. [CrossRef]
51. Léon, A.; Schild, D.; Fichtner, M. Chemical State of Ti in Sodium Alanate Doped with $TiCl_3$ using X-ray photoelectron spectroscopy. *J. Alloys Compd.* **2005**, *404*, 766–770. [CrossRef]
52. Xin, G.B.; Yang, J.Z.; Zhang, G.Q.; Zheng, J.; Li, X.G. Promising HydrogenStorage Properties and Potential Applications of Mg–Al–Pd Trilayer Films under Mild Conditions. *Dalton Trans.* **2012**, *41*, 11555–11558. [CrossRef] [PubMed]
53. Pacanowski, S.; Wachowiak, M.; Jabłoński, B.; Szymański, B.; Smardz, L. Interface Mixing and Hydrogen Absorption in Pd/Mg and Pd/Al/Mg Thin Films. *Int. J. Hydrogen Energy* **2021**, *46*, 806–813. [CrossRef]
54. Xin, G.B.; Yang, J.Z.; Wang, C.Y.; Zheng, J.; Li, X.G. Superior (De)Hydrogenation Properties of Mg–Ti–Pd Trilayer Films at Room Temperature. *Dalton Trans.* **2012**, *41*, 6783–6790. [CrossRef]
55. Fang, S.W.; Yang, Y.X.; Li, Z.L.; Chu, Y.; Chen, Y.J.; Gao, Y.; Liu, Y.X.; Cui, W.G.; Wang, X.Q.; Miao, J.; et al. Direct Mechanochemical Synthesis of Nano-$LiAlH_4$ Promoted by 0.696 wt% $TiCl_4$ Catalyst Surface-Modified Al Powder. *J. Alloys Compd.* **2024**, *1008*, 176537. [CrossRef]
56. Zang, L.; Cai, J.X.; Zhao, L.P.; Gao, W.H.; Liu, J.; Wang, Y.J. Improved Hydrogen Storage Properties of $LiAlH_4$ by Mechanical Milling with TiF_3. *J. Alloys Compd.* **2015**, *647*, 756–762. [CrossRef]

57. Saitoh, H.; Machida, A.; Katayama, Y.; Aoki, K. Formation and Decomposition of AlH_3 in the Aluminum-Hydrogen System. *Appl. Phys. Lett.* **2008**, *93*, 151918. [CrossRef]
58. Borgschulte, A.; Bielmann, M.; Züttel, A.; Barkhordarian, G.; Dornheim, M.; Bormann, R. Hydrogen Dissociation on Oxide Covered MgH_2 by Catalytically Active Vacancies. *Appl. Surf. Sci.* **2008**, *254*, 2377–2384. [CrossRef]
59. Varin, R.A.; Parviz, R. The Effects of the Nanometric Interstitial Compounds TiC, ZrC and TiC on the Mechanical and Thermal Dehydrogenation and Rehydrogenation of the Nanocomposite Lithium Alanate ($LiAlH_4$) Hydride. *Int. J. Hydrogen Energy* **2014**, *39*, 2575–2586. [CrossRef]
60. Zhai, F.Q.; Li, P.; Sun, A.Z.; Wu, S.; Wan, Q.; Zhang, W.N.; Li, Y.L.; Cui, L.Q.; Qu, X.H. Significantly Improved Dehydrogenation of $LiAlH_4$ Destabilized by $MnFe_2O_4$ Nanoparticles. *J. Phys. Chem. C* **2012**, *116*, 11939–11945. [CrossRef]
61. Ahmad, M.A.N.; Sazelee, N.A.; Ali, N.A.; Ismail, M. Enhancing the Dehydrogenation Properties of $LiAlH_4$ using K_2NiF_6 as Additive. *Int. J. Hydrogen Energy* **2022**, *47*, 24843–24851. [CrossRef]
62. Varin, R.A.; Parviz, R. The Effects of the Micrometric and Nanometric Iron (Fe) Additives on the Mechanical and Thermal Dehydrogenation of Lithium Alanate ($LiAlH_4$), its Self-Discharge at Low Temperatures and Rehydrogenation. *Int. J. Hydrogen Energy* **2012**, *37*, 9088–9102. [CrossRef]

Disclaimer/Publisher's Note: The statements, opinions and data contained in all publications are solely those of the individual author(s) and contributor(s) and not of MDPI and/or the editor(s). MDPI and/or the editor(s) disclaim responsibility for any injury to people or property resulting from any ideas, methods, instructions or products referred to in the content.